Yalin Yu
Department of Aerospace Engineering & Engineering Mechanics,
University of Texas,
Austin, TX 78712

Nikolaos Bouklas
Sibley School of Mechanical and Aerospace Engineering,
Cornell University,
Ithaca, NY 14853

Chad M. Landis
Department of Aerospace Engineering & Engineering Mechanics,
University of Texas,
Austin, TX 78712

Rui Huang[1]
Department of Aerospace Engineering & Engineering Mechanics,
University of Texas,
Austin, TX 78712
e-mail: ruihuang@mail.utexas.edu

A Linear Poroelastic Analysis of Time-Dependent Crack-Tip Fields in Polymer Gels

Based on a linear poroelastic formulation, we present an asymptotic analysis of the transient crack-tip fields for stationary cracks in polymer gels under plane-strain conditions. A center crack model is studied in detail, comparing numerical results by a finite element method to the asymptotic analysis. The time evolution of the crack-tip parameters is determined as a result of solvent diffusion coupled with elastic deformation of the gel. The short-time and long-time limits are obtained for the stress intensity factor and the crack-tip energy release rate under different chemo-mechanical boundary conditions (immersed versus not-immersed, displacement versus load controlled). It is found that, under displacement-controlled loading, the crack-tip energy release rate increases monotonically over time for the not-immersed case, but for the immersed case, it increases first and then decreases, with a long-time limit lower than the short-time limit. Under load control, the energy release rate increases over time for both immersed and not-immersed cases, with different short-time limits but the same long-time limit. These results suggest that onset of crack growth may be delayed until the crack-tip energy release rate reaches a critical value if the applied displacement or traction is subcritical but greater than a threshold. [DOI: 10.1115/1.4041040]

Keywords: polymer gel, stress intensity factor, energy release rate, delayed fracture

1 Introduction

Polymer gels have been widely used in biomedical applications [1–3]. Recently, polymer gels have been exploited as a class of soft active materials with potential applications in soft machines and soft robotics [4–7]. These applications have motivated development of smart and tough gels [8–10]. However, it remains a challenge to accurately measure fracture toughness of polymer gels [11], and fundamental understanding of the fracture mechanisms is still lacking [12]. Experimental measurements have reported a wide range of fracture toughness for polymer gels, from $\sim$1 J/m^2 for brittle gelatin and agar gels [13,14] to $\sim$9000 J/m^2 for a tough gel with hybrid alginate–polyacrylamide networks [9]. As noted by Long and Hui [11], most of these measurements were interpreted by assuming that the gels are purely elastic. On the other hand, fracture is typically rate dependent for polymer gels. For example, in an experimental study on steady-state crack growth in gelatin gels, Baumberger et al. [15] found that the effective fracture energy increased with crack velocity (so-called "velocity toughening"). They suggested viscoplastic chain pull-out as the fracture mechanism. Similarly, Lefranc and Bouchaud [13] attributed the crack velocity-dependent toughness of agar gels to viscous chain pull-out or stress accelerated chain dynamics, both localized in the crack tip region. Based on linear poroelasticity, Noselli et al. [16] predicted a poroelastic toughening effect as a result of solvent diffusion around the crack tip and proposed a poroelastic cohesive zone model for the dependence of effective toughness on crack velocity. In a recent work [17], we showed that the poroelastic toughening effect could lead to rate-dependent fracture in a long strip specimen of finite thickness, unless the crack velocity is so high that the characteristic diffusion length is much smaller than the specimen size (small-scale diffusion). In general, the rate-dependent fracture of polymer gels may result from combined effects due to the dynamic molecular processes at the crack tip (chain pull-out and bond rupture), solvent diffusion (poroelastic toughening), and polymer viscoelasticity (creep).

A related phenomenon is delayed fracture, which has been observed in experiments with polymer gels [18–20] as well as other materials [21–27]. Bonn et al. [18] proposed a thermally activated crack nucleation model for three-point bending experiments with uncracked gel specimens. Skrzeszewska et al. [19] found that the crack nucleation model could not explain their experiments with a physical gel fractured under a constant shear stress and proposed a stress-enhanced crosslink dissociation model with a rupture time decreasing exponentially with increasing stress. Based on a nonlinear visco-poroelastic model, Wang and Hong [28] suggested that the delay time depends on the size of a pre-existing crack in a similar way as diffusion-limited processes (a poroelastic effect). By assuming a specific size distribution of microcracks, they proposed a statistical theory on the lifetime prediction of a swollen gel. Recently, Tang et al. [20] conducted fracture experiments of hydrogels using precracked specimens. They observed delayed fracture when the applied energy release rate was subcritical but greater than a threshold value. The present study considers a stationary crack subject to a constant step loading by either displacement or traction control. Depending on the applied mechanical load as well as the chemical boundary conditions, the crack may grow immediately or after a delay or would never grow. Based on a linear poroelastic model, we present an asymptotic analysis on the transient crack-tip fields and determine the time-dependent stress intensity factor by a finite element method. The crack-tip energy release rate is calculated by a modified J-integral method as in previous studies [17,29], with which the scenario of delayed fracture is discussed.

Similar problems have been studied previously. Atkinson and Craster [30] analyzed the fracture behavior in linearly poroelastic media under a prescribed internal pressure and they obtained stress intensity factor as a function of time using Laplace and Fourier transforms. Hui et al. [31] studied the short-time transient fields near the tip of a stationary crack in a linearly poroelastic solid. Bouklas et al. [29] studied the effects of solvent diffusion on the crack-tip fields and the energy release rate for stationary cracks in polymer gels using a nonlinear, transient finite element

[1]Corresponding author.

Contributed by the Applied Mechanics Division of ASME for publication in the Journal of Applied Mechanics. Manuscript received June 11, 2018; final manuscript received July 26, 2018; published online August 31, 2018. Editor: Yonggang Huang.

method [32]. They proposed a modified J-integral method for calculating the transient crack-tip energy release rate for quasi-static crack growth in gels. More recently, Yang and Lin [33] presented a numerical study on the time-dependent crack-tip fields in a linearly poroviscoelastic medium under constant applied stress. Similar to Wang and Hong [28], they calculated the crack-tip energy release rate using a cohesive zone model. Alternatively, nonlinear phase-field models have been developed recently for fracture of polymer gels [34,35].

The remainder of this paper is organized as follows. Section 2 presents an asymptotic analysis based on a linear poroelastic formulation for polymer gels derived from a nonlinear theory. A center crack model is considered in Sec. 3, with the short-time and long-time limits under various chemo-mechanical conditions. Numerical results are discussed in Sec. 4. The detailed formulation for a finite element method and a crack-tip model for the short time limit are presented in appendices. Section 5 concludes the present study with a brief summary.

2 Asymptotic Analysis of Poroelastic Crack-Tip Fields

2.1 A Linear Poroelastic Formulation. Under the condition of small deformation, a linear poroelastic formulation can be derived from the generally nonlinear theory for polymer gels [36–38]. The linear formulation has allowed an asymptotic analysis of the steady-state crack-tip fields in a previous study [17]. The same linear formulation is adopted in the present study for stationary cracks. It should be noted that the deformation around a crack tip is usually large and the application of the linear formulation is, thus, limited to the region beyond a small distance away from the crack tip, assuming a small-scale nonlinear region similar to the small-scale yielding condition in linear elastic fracture mechanics. A detailed analysis on the nonlinear effects is left for future studies.

For completeness, the linear poroelastic formulation is briefly summarized as follows. Let the gel be stress free and isotropically swollen in the initial state, where the solvent in the gel has a chemical potential, $\mu = \mu_0$, in equilibrium with an external solution. Correspondingly, the initial solvent concentration in the gel is $c_0 = (1 - \lambda_0^{-3})/\Omega$, where Ω is the volume of solvent molecule and λ_0 is linear swelling ratio of the gel relative to dry state of the polymer network. The relationship between the swelling ratio (λ_0) and the chemical potential (μ_0) can be obtained from the nonlinear theory [36–38]. Considering small deformation from the initial state with a displacement field u_i, a linear strain field is defined as

$$\varepsilon_{ij} = \frac{1}{2}\left(\frac{\partial u_i}{\partial x_j} + \frac{\partial u_j}{\partial x_i}\right) \tag{2.1}$$

The volumetric part of the strain is related to the change of solvent concentration, i.e.,

$$\varepsilon_{kk} = \Omega(c - c_0) \tag{2.2}$$

where c is the solvent concentration in the deformed state.

The Cauchy stress in the gel is related to the strain and chemical potential as

$$\sigma_{ij} = 2G\left[\varepsilon_{ij} + \frac{\nu}{1-2\nu}\varepsilon_{kk}\delta_{ij}\right] - \frac{\mu - \mu_0}{\Omega}\delta_{ij} \tag{2.3}$$

where G is shear modulus and ν is Poisson's ratio,[2] both of which can be derived from the nonlinear theory [39].

The linearized mechanical equilibrium equation (assuming no body force) is

$$\frac{\partial \sigma_{ij}}{\partial x_j} = 0 \tag{2.4}$$

and the linearized rate equation for solvent diffusion is

$$\frac{\partial c}{\partial t} + \frac{\partial j_k}{\partial x_k} = 0 \tag{2.5}$$

where the diffusion flux is related to the gradient of chemical potential by a linear kinetic law

$$j_k = -M_0 \frac{\partial \mu}{\partial x_k} \tag{2.6}$$

with a constant mobility M_0 (which can be related to the solvent diffusivity in the gel [39]).

Correspondingly, the linearized boundary conditions are

$$\sigma_{ik} n_k = \tau_i \text{ and } j_k n_k = -\omega \tag{2.7}$$

where n_k is the outward unit normal vector on the boundary, τ_i is the traction, and ω is the in-flux of the solvent across the boundary.

The linearized equations can be further reduced by inserting Eq. (2.1) into Eq. (2.3) and then into Eq. (2.4)

$$\frac{\partial^2 u_i}{\partial x_j \partial x_j} + \frac{1}{1-2\nu}\frac{\partial^2 u_j}{\partial x_j \partial x_i} = \frac{1}{G\Omega}\frac{\partial \mu}{\partial x_i} \tag{2.8}$$

Substituting Eq. (2.8) into Eq. (2.6) and then into Eq. (2.5), we obtain

$$\frac{\partial c}{\partial t} = D^* \frac{\partial^2 c}{\partial x_j \partial x_j} \tag{2.9}$$

where

$$D^* = \frac{2(1-\nu)}{1-2\nu}\Omega^2 G M_0$$

is often called the effective or cooperative diffusivity [39–41]. As a standard diffusion equation, (2.9) implies a time-dependent length scale:

$$l_t = \sqrt{D^* t} \tag{2.10}$$

As in linear elasticity, the equilibrium equation (2.4) may be solved by using a stress function under the plane-strain condition. However, the poroelastic stress–strain relation in Eq. (2.3) leads to a slightly different compatibility condition, namely

$$\nabla^2 \nabla^2 \psi = -2\Omega G \nabla^2 c \tag{2.11}$$

where the Airy's stress function ψ is related to the stress components as usual

$$\sigma_\theta = \frac{\partial^2 \psi}{\partial r^2},\ \sigma_{\theta r} = -\frac{\partial}{\partial r}\left(\frac{1}{r}\frac{\partial \psi}{\partial \theta}\right),\ \text{and}\ \sigma_r = \frac{1}{r}\frac{\partial \psi}{\partial r} + \frac{1}{r^2}\frac{\partial^2 \psi}{\partial \theta^2}.$$

Therefore, under the plane-strain condition, we may solve Eq. (2.9) for the solvent concentration and then solve Eq. (2.11) for the stress function, with which both the stress and chemical potential fields can be determined [17]. For plane strain ($\varepsilon_z = 0$), we have

$$\sigma_{kk} = \nabla^2 \psi + \sigma_z \text{ and } \sigma_z = \frac{2\nu}{1-2\nu} G\Omega(c - c_0) - \frac{\mu - \mu_0}{\Omega}$$

by Eq. (2.3), so that the chemical potential is

[2]The Poisson's ratio here is often called *drained* Poisson's ratio in linear poroelasticity [30]. The *undrained* Poisson's ratio is 0.5 in the present formulation as a result of Eq. (2.2) assuming molecular incompressibility.

$$\mu = \mu_0 + \frac{G\Omega^2}{1-2\nu}(c - c_0) - \frac{\Omega}{2}\nabla^2\psi \tag{2.12}$$

2.2 Asymptotic Crack-Tip Fields. Consider a stationary crack (Fig. 1). To solve Eq. (2.9) near the crack tip ($r \to 0$), we assume

$$c = c_0 + \sum_n a_n(t) r^n f_n(\theta) \tag{2.13}$$

where r and θ are the polar coordinates with the origin at the crack tip; a_n is a function of time. Note that, since $\varepsilon_{kk} = \Omega(c - c_0)$, $n > -1$ is required in Eq. (2.13) so that the displacement remains finite at the crack tip.

Substitution of Eq. (2.13) into Eq. (2.9) leads to

$$D^* a_n(t)[f''_n(\theta) + n^2 f_n(\theta)] = a'_{n-2}(t) f_{n-2}(\theta) \tag{2.14}$$

For the crack-tip solution ($r \to 0$), the leading term in Eq. (2.13) correspond to the minimum value of n (designated as m hereafter), for which the right-hand side of Eq. (2.14) vanishes, namely

$$f''_m(\theta) + m^2 f(\theta) = 0 \tag{2.15}$$

Solving Eq. (2.15) yields

$$f_m(\theta) = b_m \cos(m\theta) + d_m \sin(m\theta) \tag{2.16}$$

Similarly, for higher order terms with $n = m + k$ and $0 < k < 2$, the right-hand side of Eq. (2.14) also vanishes and we obtain

$$f_{m+k}(\theta) = b_{m+k} \cos((m+k)\theta) + d_{m+k} \sin((m+k)\theta) \tag{2.17}$$

where k does not have to be an integer.

Additional higher-order terms can be obtained by solving Eq. (2.14) recursively with the leading terms in Eqs. (2.16) and (2.17). For example, for $n = m + 2$, we have

$$f''_{m+2}(\theta) + (m+2)^2 f_{m+2}(\theta) = [b_m \cos(m\theta) + d_m \sin(m\theta)]q \tag{2.18}$$

$$a'_m(t) = qD^* a_{m+2}(t) \tag{2.19}$$

where q is a constant to be determined. Solving Eq. (2.18), we obtain

$$f_{m+2}(\theta) = \frac{q}{4(m+1)}[b_m \cos(m\theta) + d_m \sin(m\theta)] + b_{m+2} \cos[(m+2)\theta] + d_{m+2} \sin[(m+2)\theta] \tag{2.20}$$

Therefore, the leading terms for the solvent concentration can be written as

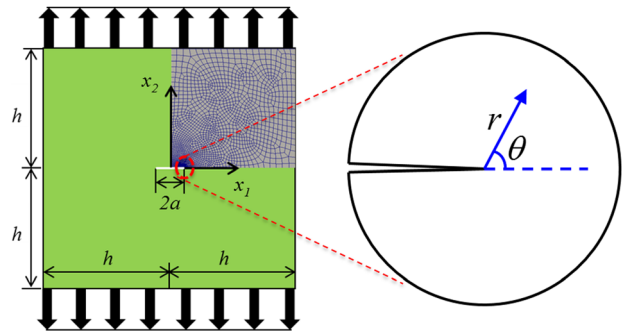

Fig. 1 Schematic of a center-cracked specimen under tension. A polar coordinate at the crack tip is used for the asymptotic crack-tip fields. A finite element mesh is shown for one quarter of the specimen.

$$c = c_0 + \sum_{0 \le k \le 2} a_{m+k}(t) r^{m+k} f_{m+k}(\theta) + \cdots \tag{2.21}$$

With Eq. (2.21) for the solvent concentration, Eq. (2.11) becomes

$$\nabla^2\nabla^2\psi = -2\Omega G q a_{m+2}[b_m \cos(m\theta) + d_m \sin(m\theta)]r^m \tag{2.22}$$

The general solution to Eq. (2.22) consists of a particular solution and a homogeneous solution, namely

$$\psi = \psi_h(r,\theta) - \frac{\Omega G q a_{m+2}}{16(m+1)(m+2)}[b_m \cos(m\theta) + d_m \sin(m\theta)]r^{m+4} \tag{2.23}$$

where the homogenous solution takes the form of a series expansion as

$$\psi_h(r,\theta) = \sum_{n=1}^{\infty} \psi_n(\theta) r^{\frac{n+2}{2}} \tag{2.24}$$

$$\psi_n(\theta) = C_{n1} \cos\left(\frac{n+2}{2}\theta\right) + C_{n2} \sin\left(\frac{n+2}{2}\theta\right) + C_{n3} \cos\left(\frac{n-2}{2}\theta\right) + C_{n4} \sin\left(\frac{n-2}{2}\theta\right) \tag{2.25}$$

The stress field corresponding to the particular solution is non-singular, $\sigma \sim r^{m+2}$ ($m > -1$). As a result, the leading terms for the stress function are from the homogenous solution with $1 \le n \le 4$, which takes the same form as the linear elastic crack-tip solution.

The asymptotic solution in the form of Eqs. (2.21) and (2.23) can be decomposed into symmetric (mode I) and antisymmetric (mode II) modes with respect to the angular variations. Hereafter, we consider only the solution for cracks in the symmetric mode (mode I) under plane strain conditions. Keeping the four leading terms for mode I, the stress function becomes

$$\psi(r,\theta,t) = \sum_{n=1}^{4} r^{\frac{n+2}{2}} \left[C_{n1}(t)\cos\left(\frac{n+2}{2}\theta\right) + C_{n3}(t)\cos\left(\frac{n-2}{2}\theta\right)\right] + \cdots \tag{2.26}$$

and the solvent concentration can be written as

$$c(r,\theta,t) = c_0 + \sum_{0 \le k < 2} a_{m+k}(t) r^{m+k} \cos(m+k)\theta + \cdots \tag{2.27}$$

where the higher order term ($\sim r^{m+2}$) in Eq. (2.21) has been ignored.

For plane-strain problems, the chemical potential is obtained by inserting Eqs. (2.26) and (2.27) into Eq. (2.12)

$$\frac{\mu - \mu_0}{\Omega} = \frac{\Omega G}{1-2\nu} \sum_{0 \le k < 2} a_{m+k} r^{m+k} \cos(m+k)\theta - \sum_{n=1}^{4} n C_{n3} r^{\frac{n-2}{2}} \cos\left(\frac{n-2}{2}\theta\right) + \cdots \tag{2.28}$$

If the crack is filled with an external solution (e.g., water), the chemical potential at the crack faces ($\theta = \pm\pi$) equals a constant, i.e., $\mu = \mu_0 = 0$; we call such a crack as "immersed." Alternatively, if the crack is not immersed and the crack faces are impermeable to solvent diffusion, the flux across the crack faces is zero, i.e., $(\partial\mu/\partial\theta) = 0$. In Eq. (2.28), the first leading term from the

stress function is proportional to $r^{-1/2}$ $(n=1)$, which is singular as $r \to 0$. Because the chemical potential is non-singular at the crack tip, the leading term of the solvent concentration must have the same order of singularity as the stress field, i.e., $m = -1/2$. Moreover, to satisfy the boundary conditions for the chemical potential at the crack faces (immersed or not-immersed), we must have $k = (n-1)/2$ for the four leading terms of the solvent concentration to have the same orders as $\nabla^2\psi$ with $1 \le n \le 4$. Thus, Eq. (2.27) can be rewritten as

$$c(r,\theta,t) = c_0 + \sum_{n=1}^{4} c_n(t) r^{\frac{n-2}{2}} \cos\left(\frac{n-2}{2}\theta\right) + \cdots \tag{2.29}$$

Then, the leading terms for the chemical potential in Eq. (2.28) becomes

$$\mu(r,\theta,t) = \mu_0 + \sum_{n=1}^{4} \mu_n(t) r^{\frac{n-2}{2}} \cos\left(\frac{n-2}{2}\theta\right) + \cdots \tag{2.30}$$

where $\mu_n(t) = G\Omega/(1-2\nu)c_n(t) - nC_{n3}(t)$. For the singular term $(n=1)$ to vanish in Eq. (2.30), it requires that $\mu_1 = 0$ and hence

$$\frac{G\Omega}{1-2\nu} c_1 - C_{13} = 0 \tag{2.31}$$

With the chemical potential in Eq. (2.30), the chemical boundary condition for the immersed case $(\mu_0 = 0)$ requires that $\mu_2 = \mu_4 = 0$ and hence

$$\frac{G\Omega}{1-2\nu} c_2 - 2C_{23} = 0 \tag{2.32}$$

$$\frac{G\Omega}{1-2\nu} c_4 - 4C_{43} = 0 \tag{2.33}$$

As a result, the chemical potential in this case becomes

$$\mu = \mu_3(t)\sqrt{r}\cos\left(\frac{\theta}{2}\right) + \cdots \tag{2.34}$$

For the not-immersed case, the zero flux boundary condition requires that $\mu_3 = 0$ and hence

$$\frac{G\Omega}{1-2\nu} c_3 - 3C_{33} = 0 \tag{2.35}$$

The leading terms of the chemical potential are constant and linear $(n = 2, 4)$

$$\mu = \mu_{\text{tip}}(t) + \mu_4(t) r\cos\theta + \cdots \tag{2.36}$$

where $\mu_{\text{tip}}(t) = \mu_0 + \mu_2(t)$. This is different from the asymptotic solution for the case of a steady-state crack [17].

With the Airy stress function in Eq. (2.26), the stress components are obtained as follows:

$$\sigma_{rr} = -\frac{1}{4}\sum_{n=1}^{4} r^{\frac{n-2}{2}}\left[n(n+2)C_{n1}\cos\left(\frac{n+2}{2}\theta\right) + n(n-6)C_{n3}\cos\left(\frac{n-2}{2}\theta\right)\right] + \cdots \tag{2.37a}$$

$$\sigma_{\theta\theta} = \frac{1}{4}\sum_{n=1}^{4} r^{\frac{n-2}{2}}\left[n(n+2)C_{n1}\cos\left(\frac{n+2}{2}\theta\right) + n(n+2)C_{n3}\cos\left(\frac{n-2}{2}\theta\right)\right] + \cdots \tag{2.37b}$$

$$\sigma_{r\theta} = \frac{1}{4}\sum_{n=1}^{4} r^{\frac{n-2}{2}}\left[n(n+2)C_{n1}\sin\left(\frac{n+2}{2}\theta\right) + n(n-2)C_{n3}\sin\left(\frac{n-2}{2}\theta\right)\right] + \cdots \tag{2.37c}$$

which are identical to the linear elastic crack-tip solution. To satisfy the traction-free boundary conditions at the crack faces, it requires: $C_{11} = C_{13}/3$, $C_{21} = -C_{23}$, $C_{31} = -C_{33}/5$, $C_{41} = -C_{43}$. Following the linear elastic fracture mechanics, the two leading terms of stresses are related to the stress intensity factor (K_I) and the T-stress (σ_T) as: $C_{13} = K_I/\sqrt{2\pi}$, $C_{23} = \sigma_T/4$. Thus, the stress components can be written as

$$\sigma_{ij} = \frac{K_I}{\sqrt{2\pi r}} f_{ij}(\theta) + \sigma_T \delta_{1i}\delta_{1j} + \cdots \tag{2.38}$$

where

$$f_{11} = \cos\left(\frac{\theta}{2}\right)\left[1 - \sin\left(\frac{\theta}{2}\right)\sin\left(\frac{3\theta}{2}\right)\right] \tag{2.39a}$$

$$f_{22} = \cos\left(\frac{\theta}{2}\right)\left[1 + \sin\left(\frac{\theta}{2}\right)\sin\left(\frac{3\theta}{2}\right)\right] \tag{2.39b}$$

$$f_{12} = \cos\left(\frac{\theta}{2}\right)\sin\left(\frac{\theta}{2}\right)\cos\left(\frac{3\theta}{2}\right) \tag{2.39c}$$

With Eq. (2.31), the singular term for the solvent concentration is related to the stress intensity factor as

$$c_1 = \frac{(1-2\nu)K_I}{\Omega G\sqrt{2\pi}} \tag{2.40}$$

which is true for both the immersed and not-immersed cases. The next term for the solvent concentration is a constant $(n=2)$ that can be related to the T-stress and the crack-tip chemical potential as:

$$c_2 = \frac{1-2\nu}{\Omega G}\left(\frac{\mu_{\text{tip}}}{\Omega} + \frac{\sigma_T}{2}\right) \tag{2.41}$$

where $\mu_{\text{tip}} = 0$ for the immersed case.

Furthermore, the singular part of the crack-tip strain field is identical to that in the linear elastic case, and the leading term of the displacement field is also identical. In particular, the near-tip crack-opening displacement is

$$u_2(r, \theta = \pm\pi) = \pm\frac{2(1-\nu)K_I}{G}\sqrt{\frac{r}{2\pi}} + \cdots \tag{2.42}$$

In summary, we have obtained a linear poroelastic solution for the asymptotic crack-tip fields (mode I), with the crack-tip stress components given by Eqs. (2.38) and the solvent concentration by Eq. (2.29). The chemical potentials are given by Eqs. (2.34) and (2.36) for the immersed and not-immersed cases, respectively. The leading terms of the poroelastic crack-tip fields require three independent crack-tip parameters for the immersed case: K_I, σ_T, μ_3, but require 4 independent parameters for the not-immersed case: $K_I, \sigma_T, \mu_{tip}, \mu_4$. All these parameters are time dependent for a stationary crack in a linearly poroelastic material, and they can be determined numerically for specific specimen geometry and loading conditions.

2.3 Energy Release Rate. To calculate energy release rate for crack growth in a poroelastic material, a modified J-integral

was derived by Bouklas et al. [29] in a nonlinear setting, which can be linearized to yield [17]:

$$J^* = \int_\Gamma \left(\hat{\phi} n_1 - \sigma_{ij} n_j \frac{\partial u_i}{\partial x_1} \right) d\Gamma + \int_A (c - c_0) \frac{\partial \mu}{\partial x_1} dA \tag{2.43}$$

where A is the area enclosed by the contour Γ around the crack tip and the linearized free energy density function is

$$\hat{\phi} = G\left[\varepsilon_{ij}\varepsilon_{ij} + \frac{\nu}{1-2\nu}(\varepsilon_{kk})^2 \right] - (\mu - \mu_0)(c - c_0) \tag{2.44}$$

The modified J-integral is path independent and can be calculated by the domain integral method, as shown in the previous studies [17,29]. Note that the linearized J-integral in Eq. (2.43) gives the energy release rate per unit area of crack growth in the initial swollen state, not in the dry state as in the original definition by Bouklas et al. [29]; the two are simply related by a factor of λ_0^2.

Similar to the case of steady-state crack growth [17], the energy release rate by the modified J-integral can be related to the crack-tip stress intensity factor for a stationary crack as

$$J^* = \frac{1-\nu}{2G} K_I^2 \tag{2.45}$$

which can be shown as a result of the asymptotic crack-tip fields. Since K_I is a function of time, the energy release rate J^* is also a function of time for a stationary crack in a poroelastic material.

3 A Center Crack Model

Consider a specimen with a center crack (Fig. 1), subject to uniaxial tension by either displacement or load (traction) controlled step loading under plane strain conditions. The initial state of the gel is stress free and homogeneously swollen, with a solvent concentration $c_0 = (1 - \lambda_0^{-3})/\Omega$ corresponding to the chemical potential $\mu_0 = 0$. The specimen may be immersed in an external solution so that all the boundaries (including the crack faces) are in contact with the external solution with a chemical potential $\mu = 0$. Alternatively, if the specimen is not immersed, we assume that all the boundaries are impermeable to solvent diffusion so that the normal flux is zero. The same problem was considered by Bouklas et al. [29] using a nonlinear formulation, which did not permit an asymptotic analysis. Here, based on the linear poroelasticity formulation (Sec. 2.1), a simpler finite element method is developed to solve the initial/boundary value problem (Appendix A), which allows us to compare with the asymptotic analysis and determine the time-dependent crack-tip parameters as well as the crack-tip energy release rate.

By symmetry, only a quarter of the specimen is modeled by the finite element method as illustrated in Fig. 1. The symmetry boundary conditions are imposed at $x_1 = 0$ and at $x_1 > a$, $x_2 = 0$. The remote tension under displacement control is applied as

$$u_2 = h\varepsilon_h,\ \sigma_{12} = 0 \text{ at } x_2 = h \tag{3.1}$$

Under load (traction) control, the boundary condition becomes[3]

$$\sigma_2 = \sigma_h,\ \sigma_{12} = 0 \text{ at } x_2 = h \tag{3.2}$$

Traction-free conditions are assumed for the crack face ($x_1 < a$, $x_2 = 0$) and at $x_1 = h$. The applied strain (ε_h) or stress (σ_h) is assumed to be a constant for $t > 0$ (step loading).

For the finite element analysis, all the lengths are normalized by half of the crack length (e.g., setting $a = 1$) and time is normalized by the characteristic diffusion time, $\tau = a^2/D^*$. Stresses are normalized by the shear modulus G, chemical potential by $G\Omega$ and solvent concentration by Ω^{-1}. Within the linear poroelastic formulation, the elastic moduli (G and ν) are related to the gel properties. Taking $\lambda_0 = 3.215$ as the initial swelling ratio, the corresponding Poisson's ratio is 0.24. The Poisson's ratio can be varied by using different gel properties with different initial swelling ratios [39].

By dimensional considerations, the poroelastic stress intensity factor at the crack tip can be written as

$$K_I = \xi_u\left(\frac{t}{\tau}, \frac{h}{a}, \nu\right) G\varepsilon_h \sqrt{\pi a} \tag{3.3a}$$

or

$$K_I = \xi_\sigma\left(\frac{t}{\tau}, \frac{h}{a}, \nu\right) \sigma_h \sqrt{\pi a} \tag{3.3b}$$

where ξ_u and ξ_σ are dimensionless functions under displacement and traction controlled conditions, respectively.

For a linearly elastic specimen of the same geometry as in Fig. 1, the stress intensity factor is

$$K_e = \xi_{ue}\left(\frac{h}{a}\right) \frac{2G\varepsilon_h}{1-\nu} \sqrt{\pi a} \text{ (displacement control)} \tag{3.4a}$$

or

$$K_e = \xi_{\sigma e}\left(\frac{h}{a}\right) \sigma_h \sqrt{\pi a} \text{ (traction control)} \tag{3.4b}$$

For $h/a = 10$, we obtain numerically $\xi_{ue}(10) = 0.989$ and $\xi_{\sigma e}(10) = 1.014$, both of which approaches 1 as $h/a \to \infty$.

Instantaneously upon a step loading ($t = 0^+$), if the poroelastic material behaves like an incompressible elastic material with $\nu = 0.5$ (undrained), the stress intensity factor would be (for both immersed and not-immersed cases): $K_{I0} = 4\xi_{ue} G\varepsilon_h \sqrt{\pi a}$ (displacement control) or $K_{I0} = \xi_{\sigma e}\sigma_h\sqrt{\pi a}$ (load control). Correspondingly, the energy release rate would be: $J_0 = (K_{I0}^2/4G)$. However, even for an infinitely small time ($t \to 0^+$), there exists a diffusion zone around the crack tip, which may influence the stress intensity factor and the crack-tip energy release rate. As shown in the following (Table 1), the short-time limits for the stress intensity factor and the energy release rate for a poroelastic material are not necessarily the same as those expected for an incompressible elastic material.

The instantaneous elastic deformation around the crack leads to an inhomogeneous field of chemical potential, which drives solvent diffusion. As the poroelastic stress intensity factor evolves over time (Eq. 3.3), the crack-tip energy release rate by the modified J-integral can be written as

$$\frac{J^*}{J_0} = \Lambda\left(\frac{t}{\tau}, \frac{h}{a}, \nu\right) \tag{3.5}$$

where the dimensionless function on the right-hand side is to be determined numerically and depends on the chemo-mechanical conditions.

Next, we discuss the short-time and long-time limits for the stress intensity factor and the energy release rate under different chemo-mechanical conditions, followed by the full-field numerical results and discussion in Sec. 4.

3.1 Short-Time Limits. At the short time limit ($0 < t/\tau \ll 1$), solvent diffusion is confined in a small region around the crack tip (as well as near the edges) with a length scale, $l_t = \sqrt{D^* t} \ll a$. In this crack-tip region ($r < l_t$), the stress is partly relaxed, leading to a reduced stress intensity factor, referred to as poroelastic shielding [30,31]. For the immersed case, an

[3]In experiments the load may be applied by a dead weight, in which case the traction at $x_2 = h$ may not be uniform unless $h \gg a$.

Table 1 Short-time and long-time limits of the poroelastic stress intensity factor and the crack-tip energy release rate for center-cracked specimens

		Short-time limit	Long-time limit
Immersed	Displacement control	$K_I(t\to 0^+)=K_{I0}\left[\frac{1}{2(1-\nu)}\right]^{0.735}, J^*(t\to 0^+)=J_0\left[\frac{1}{2(1-\nu)}\right]^{0.47}$	$K_I(t\to\infty)=\frac{K_{I0}}{2(1-\nu)}, J^*(t\to\infty)=\frac{J_0}{2(1-\nu)}$
	Load control		$K_I(t\to\infty)=K_{I0}, J^*(t\to\infty)=2(1-\nu)J_0$
Not-immersed	Displacement control	$K_I(t\to 0^+)=K_{I0}\sqrt{\frac{1}{2(1-\nu)}}, \quad J^*(t\to 0^+)=J_0$	$K_I(t\to\infty)=0.993K_{I0}, J^*(t\to\infty)=1.496J_0$[5]
	Load control		$K_I(t\to\infty)=K_{I0}, J^*(t\to\infty)=2(1-\nu)J_0$

approximate analytical solution was presented by Hui et al. [31], which predicted a relation between the poroelastic crack-tip stress intensity factor and the instantaneous (elastic) stress intensity factor

$$K_I(t\to 0^+)=\frac{K_{I0}}{2(1-\nu)} \tag{3.6}$$

On the other hand, Atkinson and Craster [30] presented a more sophisticate analysis and predicted a different relation for the immersed case

$$K_I(t\to 0^+)=\frac{K_{I0}}{[N_+(0)-\bar{\eta}d]} \tag{3.7}$$

where $N_+(0)$, $\bar{\eta}$, and d are functions of Poisson's ratio (see Appendix B). It is found that the numerical results of Eq. (3.7) can be written approximately as

$$K_I(t\to 0^+)=K_{I0}\left[\frac{1}{2(1-\nu)}\right]^{\alpha} \tag{3.8}$$

where $\alpha\approx 0.735$ (see Appendix C). As shown in Fig. 11, results from our finite element analysis agree closely with Eq. (3.8), whereas Eq. (3.6) underestimates the crack-tip stress intensity factor. Interestingly, a relation identical to Eq. (3.6) was recently predicted for the case of steady-state crack growth in a linearly poroelastic material at the limits of fast or slow crack speed [17].

For not-immersed cases, Craster and Atkinson [42] obtained the short-time limit of the crack-tip stress intensity factor as

$$K_I(t\to 0^+)=K_{I0}\sqrt{\frac{1}{2(1-\nu)}} \tag{3.9}$$

Therefore, in both immersed and not-immersed cases, $K_I(t\to 0^+)<K_{I0}$ as long as $\nu<0.5$; the poroelastic shielding is slightly weaker for the not-immersed case.

With Eq. (2.45), the crack-tip energy release rate at the short-time limit is obtained for the immersed and not-immersed cases as

$$J^*(t\to 0^+)=J_0\left(\frac{1}{2(1-\nu)}\right)^{2\alpha-1} \tag{3.10}$$

Thus, for the immersed case ($\alpha\approx 0.735$), $J^*(t\to 0^+)<J_0$; for the not-immersed case ($\alpha=0.5$), $J^*(t\to 0^+)=J_0$. Interestingly, while poroelastic shielding in terms of the stress intensity factor is predicted for both cases, poroelastic toughening in terms of the energy release rate is predicted for the immersed case only. As noted by Eqs. (2.34) and (2.36), while the chemical potential is non-singular at the crack tip for both immersed and not-immersed cases, the gradient of chemical potential is singular for the immersed case but not singular for the not-immersed case. As a result, the energy dissipation due to solvent diffusion as calculated by the domain integral in Eq. (2.43) approaches zero at the short-time limit for the not-immersed case but approaches a finite value for the immersed case, hence the difference in poroelastic toughening.

The poroelastic crack-tip stress intensity factor and energy release rate at the short-time limit are the same for displacement or load control except for the different values from the elastic solution (K_{I0} and J_0).

3.2 Long-Time Limits. At the long-time limit ($t\to\infty$), the chemical potential becomes homogenous so that the specimen reaches both chemical and mechanical equilibrium. For the immersed case, the chemical potential is zero ($\mu=\mu_0=0$), while for the not-immersed case it is a constant ($\mu=\mu_\infty$) that depends on the applied displacement or traction. In both cases, the right-hand side of Eq. (2.11) vanishes,[4] and the poroelasticity problem becomes identical to an elasticity problem. For the immersed case, the stress intensity factor at the long-time limit is exactly the same as the elastic case with the (drained) Poisson's ratio (ν). Under displacement control, we obtain:

$$K_I(t\to\infty)=\frac{K_{I0}}{2(1-\nu)} \tag{3.11}$$

which is smaller than the short-time limit given by Eq. (3.8) with $\nu<0.5$. Incidentally, this is the same as the short-time limit predicted by Hui et al. [31]. Under load control, the elastic stress intensity factor is independent of Poisson's ratio. As a result, the poroelastic stress intensity factor at the long time limit is simply

$$K_I(t\to\infty)=K_{I0}=\xi_{\sigma\epsilon}\sigma_h\sqrt{\pi a} \tag{3.12}$$

which is greater than the short-time limit in Eq. (3.8) for the immersed case. Therefore, the poroelastic stress intensity factor as a function of time depends on the loading conditions, with different long-time limits for displacement and load control.

With Eq. (2.45), the crack-tip energy release rate at the long-time limit for the immersed case is obtained as

$$J^*(t\to\infty)=\frac{J_0}{2(1-\nu)} \tag{3.13a}$$

under displacement control and

$$J^*(t\to\infty)=2(1-\nu)J_0 \tag{3.13b}$$

under load control. Similar to the stress intensity factor, the crack-tip energy release rate as a function of time also depends on the loading conditions.

For the not-immersed case, under load control, the stress field is the same as that for the immersed cases since it is subject to only traction boundary conditions, although the strain field is different due to different chemical potential in the stress–strain relation

[4]Note that, by Eq. (2.8), $\nabla^2 c=(1-2\nu/2(1-\nu)\Omega^2 G)\nabla^2\mu$, which vanishes at the long-time limit.

[5]Based on numerical results for $h/a=10$ and $\nu=0.24$.

(Eq. 2.3). Thus, the stress intensity factor in this case is the same as Eq. (3.12), which again is greater than the short-time limit in Eq. (3.9) for the not-immersed case. Under displacement control, the traction-free boundary condition at the crack faces and the free edge ($x_1 = h$) requires that

$$2G\left(\varepsilon_{ij} + \frac{\nu}{1-2\nu}\varepsilon_{kk}\delta_{ij}\right)n_j = \frac{\mu_\infty - \mu_0}{\Omega}n_i \tag{3.14}$$

Comparing to the immersed case, the only difference is that the right-hand side of Eq. (3.14) is not zero for the not-immersed case. Thus, the long-time limit for the not-immersed case under displace control can be regarded as a superposition of two elasticity problems as illustrated in Fig. 2: one corresponding to the long-time limit for the immersed case with the same applied displacement (problem A) and the other (problem B) with zero applied displacement, but with a normal traction or pressure, $p = -(\mu_\infty - \mu_0/\Omega)$, acting on the crack faces and the free edges ($x_1 = h$). By linear superposition, the stress intensity factor at the long-time limit in this case can be obtained as

$$K_I(t \to \infty) = \frac{K_{I0}}{2(1-\nu)} + K_p \tag{3.15}$$

where K_p is the stress intensity factor in problem B. Since $\mu_\infty - \mu_0 < 0$ under tension, the crack face in problem B is subject to a positive pressure ($p > 0$), which gives a positive stress intensity factor ($K_p > 0$). Hence, the stress intensity factor at the long-time limit is greater for the not-immersed case than the immersed case under displacement control.

Furthermore, the chemical potential at the long time limit for the not-immersed case can be determined semi-analytically as follows. Since the corresponding poroelasticity problem can be treated as a superposition of the two linear elasticity problems (Fig. 2), the pressure for problem B must be chosen such that the sum of the total volume changes in the two elasticity problems is zero because the total volume of the specimen is conserved for the not-immersed case. Let the average normal traction at the top/bottom edges of the two elasticity problems be

$$\bar{\sigma}_{22} = \frac{1}{2h}\int_{-h}^{h}\sigma_{22}dx \tag{3.16}$$

It can be shown that $\bar{\sigma}^A_{22} = 2G\varepsilon_h/(1-\nu)$ and $\bar{\sigma}^B_{22} = -\nu p/(1-\nu)$ if $h/a \gg 1$. For $h/a = 10$ and $\nu = 0.24$, by a standard finite element method, we obtain $\bar{\sigma}^A_{22} = 2.60\,G\varepsilon_h$ and $\bar{\sigma}^B_{22} = -0.33p$, both of which are close to those for $h/a \gg 1$. For the same specimen subject to a uniform equibiaxial compressive stress ($\sigma_{11} = \sigma_{22} = \sigma_0 < 0$) under the plane-strain condition, the resulting strains in the x_1-and x_2-directions are the same ($\varepsilon_{11} = \varepsilon_{22} = \varepsilon_0$). Then, by the reciprocal theorem, the volume changes in the linear elasticity problems A and B can be obtained as

$$\sigma_0\Delta V_A = (2h\bar{\sigma}^A_{22})(2h\varepsilon_0) \tag{3.17a}$$

$$\sigma_0\Delta V_B = (2h\bar{\sigma}^B_{22})(2h\varepsilon_0) - (2hp)(2h\varepsilon_0) \tag{3.17b}$$

Thus, by setting $\Delta V_A + \Delta V_B = 0$, we obtain $p = \bar{\sigma}^A_{22} + \bar{\sigma}^B_{22}$ and hence for $h/a \gg 1$, $p = 2G\varepsilon_h$ and $\mu_\infty = \mu_0 - 2\Omega G\varepsilon_h$. For $h/a = 10$, we obtain numerically $p = 1.95\,G\varepsilon_h$. The corresponding stress intensity factor for problem B is $K_p = (p + \bar{\sigma}^B_{22})\sqrt{\pi a} = 2(1-2\nu)/(1-\nu)G\varepsilon_h\sqrt{\pi a}$ for $h/a \gg 1$ or in general, $K_p = \xi_p(h/a,\nu)G\varepsilon_h\sqrt{a}$, where $\xi_p = 2.34$ for $h/a = 10$ and $\nu = 0.24$. Therefore, for the not-immersed case under displacement control, the crack-tip stress intensity factor at the long-time limit is

$$K_I(t \to \infty) = \frac{K_{I0}}{2(1-\nu)} + K_p = K_{I0} \text{ for } h/a \gg 1 \tag{3.18}$$

and $K_I(t \to \infty) = 0.993K_{I0}$ for $h/a = 10$ and $\nu = 0.24$. We note that the long-time limits under displacement and load control conditions are the same for the not-immersed case if $h/a \gg 1$, but slightly different for a finite specimen. Similarly, the energy release rate at the long-time limit for $h/a \gg 1$ is the same as Eq. (3.13*b*) for the not-immersed case under displacement control, but slightly different for a finite specimen: $J^*(t \to \infty) = 1.496J_0$ for $h/a = 10$ and $\nu = 0.24$.

For a not-immersed specimen under load control, the long-time limit of the chemical potential can be obtained in the same way by the reciprocal theorem: $\mu_\infty = \mu_0 - 0.5\sigma_h\Omega$, which is the same as that under displacement control for $h/a \gg 1$ (with $\sigma_h = 4G\varepsilon_h$).

Table 1 summarizes the short-time and long-time limits of the poroelastic stress intensity factor and the crack-tip energy release rate for the immersed and not-immersed cases under displacement and load controlled conditions. Notably, while the long-time limits of the stress intensity factor and energy release rate are lower than their short-time limits for the immersed case under displacement control, it is the opposite for the other three cases (immersed load control, and not-immersed, both displacement and load control). In particular, under displacement control, the lower long-time limit for the immersed case may be expected as a result of poroelastic relaxation, which however is not the case for the not-immersed specimen. Under load control, the long-time limits are higher for both immersed and not-immersed cases, similar to the creep behavior in metals and polymers.

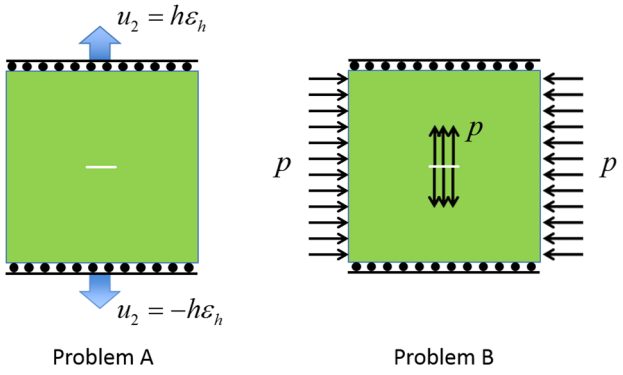

Fig. 2 Superposition of two linear elasticity problems (A and B) for the long-time limit of the not-immersed case under displacement control

4 Numerical Results and Discussion

In this section, we present numerical results for the center-crack model (Fig. 1) obtained by the finite element method (Appendix A) based on linear poroelasticity. We compare the numerical results with the asymptotic analysis for the crack-tip fields as predicted in Sec. 2.2 and determine the time-dependent crack-tip parameters. The short-time and long-time limits as well as the transient evolution in between are examined for different chemical and mechanical boundary conditions (immersed versus not-immersed, displacement versus load control). The possible scenario of delayed fracture as a result of solvent diffusion is discussed based on a hypothetic criterion for onset of crack growth.

4.1 Poroelastic Crack-Tip Fields. The asymptotic poroelastic crack-tip fields are derived in Sec. 2.2 for both the immersed and not-immersed cases. The singular stress and solvent concentration fields are given in Eqs. (2.38) and (2.29), where the leading terms relate to the stress intensity factor and T-stress. As discussed in Sec. 3, the stress intensity factor is a function of time (Eq. 3.3) and can be determined numerically. For a center-cracked

specimen with $h/a = 10$ and $\nu = 0.24$, Fig. 3 shows the numerical results at $t/\tau = 10^{-4}$ for the immersed case, comparing the angular distributions of the stress and solvent concentration with the asymptotic predictions. A small strain, $\varepsilon_h = 0.001$, is applied (displacement control) for the numerical calculation, but the normalized results are independent of the applied strain by the linear theory. By fitting the angular distribution of the stress component σ_{22} in Fig. 3(*a*) (or σ_{12} in Fig. 3(*b*)), a stress intensity factor is obtained, $K_I = 5.23\, G\varepsilon_h\sqrt{a}$, which is close to the short-time limit by Eq. (3.8) for this case, $K_I(t \to 0^+) = 5.15\, G\varepsilon_h\sqrt{a}$. Next, the T-stress, $\sigma_T = -7.87\, G\varepsilon_\infty$, can be obtained by fitting of σ_{11} in Fig. 3(*c*). Correspondingly, by Eqs. (2.40) and (2.41), we obtain $\Omega c_1 = 1.085\varepsilon_h\sqrt{a}$ and $\Omega c_2 = -2.05\varepsilon_h$, with which the predicted angular distribution of the solvent concentration by the two leading terms in Eq. (2.29) is in excellent agreement with the numerical result (Fig. 3(*d*)). The numerical results at different radii (close to the crack tip) are plotted to show that the angular distributions are independent of the radius as predicted for the singular crack-tip fields. The agreement confirms the square-root singularity for both the stress and concentration fields.

Similar numerical results are obtained for the not-immersed case at $t/\tau = 10^{-4}$, for which the stress intensity factor is found to be slightly larger: $K_I = 5.70\, G\varepsilon_\infty\sqrt{a}$, as expected for the short-time limit by Eq. (3.9), $K_I(t \to 0^+) = 5.69\, G\varepsilon_h\sqrt{a}$. In this case, the T-stress and Ωc_2 are obtained independently by fitting the stress component σ_{11} and the solvent concentration: $\sigma_T = -6.01\, G\varepsilon_\infty$ and $\Omega c_2 = -8.63\varepsilon_\infty$. Then, by Eq. (2.41), we obtain $\mu_{\text{tip}} = -13.6\Omega G\varepsilon_h$ as the chemical potential at the crack tip (as opposed to $\mu_{\text{tip}} = 0$ for the immersed case). Figure 4 shows the angular distributions of the chemical potential for the immersed and not-immersed cases. As predicted by Eq. (2.34), the leading term of the chemical potential for the immersed case is proportional to $\sqrt{r}$. By fitting the numerical results with the analytical prediction, we obtain $\mu_3 = -150\Omega G\varepsilon_\infty/\sqrt{a}$. For the not-immersed case, Eq. (2.36) predicts a constant term μ_{tip} as the leading term, which is related to the T-stress and c_2 by Eq. (2.41). By subtracting the constant μ_{tip}, the next leading term is proportional to r, for which we obtain $\mu_4 = -494\, G\Omega\varepsilon_\infty/a$ by fitting. Note that in Fig. 4 the chemical potentials for the two cases are normalized differently. The slope of the chemical potential is zero at $\theta = \pi$ for the not-immersed case as required by the zero-flux condition at the crack face, whereas the slope is not zero for the immersed case, indicating solvent flux across the crack face. Again, the numerical results at different radii are plotted to show that the angular distributions are independent of the radius as predicted.

Figures 3 and 4 illustrate that the time-dependent crack-tip parameters can be determined by comparing the numerical results for the angular distributions of stress, solvent concentration, and chemical potential to the asymptotic predictions. In particular, for the immersed case, three independent parameters are determined for the poroelastic crack-tip fields, including K_I, σ_T and μ_3, while four independent parameters are determined for the not-immersed case, including K_I, σ_T, μ_{tip} and μ_4. As noted by Yu et al. [17] for steady-state crack growth in a linearly poroelastic material, it is also possible to determine the crack-tip parameters from the radial distributions of the displacement and chemical potential along the crack face. For example, the stress intensity factor can be determined by the crack-opening displacement based on Eq. (2.42). Figure 5 shows the normalized crack-tip parameters versus the normalized time for the center-cracked specimen with $h/a = 10$ and $\nu = 0.24$. The stress intensity factor (Fig. 5(*a*)) for the not-immersed case increases monotonically with time from the short-time limit ($K_I(t \to 0^+) = 5.69\, G\varepsilon_h\sqrt{a}$) to the long-time limit ($K_I(t \to \infty) = 6.96\, G\varepsilon_h\sqrt{a}$). On the other hand, the stress intensity factor for the immersed case first increases and then decreases over time, with a peak at $t/\tau \sim 1$. The non-monotonic variation may be attributed to the effect of solvent diffusion from the outer boundary for the immersed case, consistent with previous results

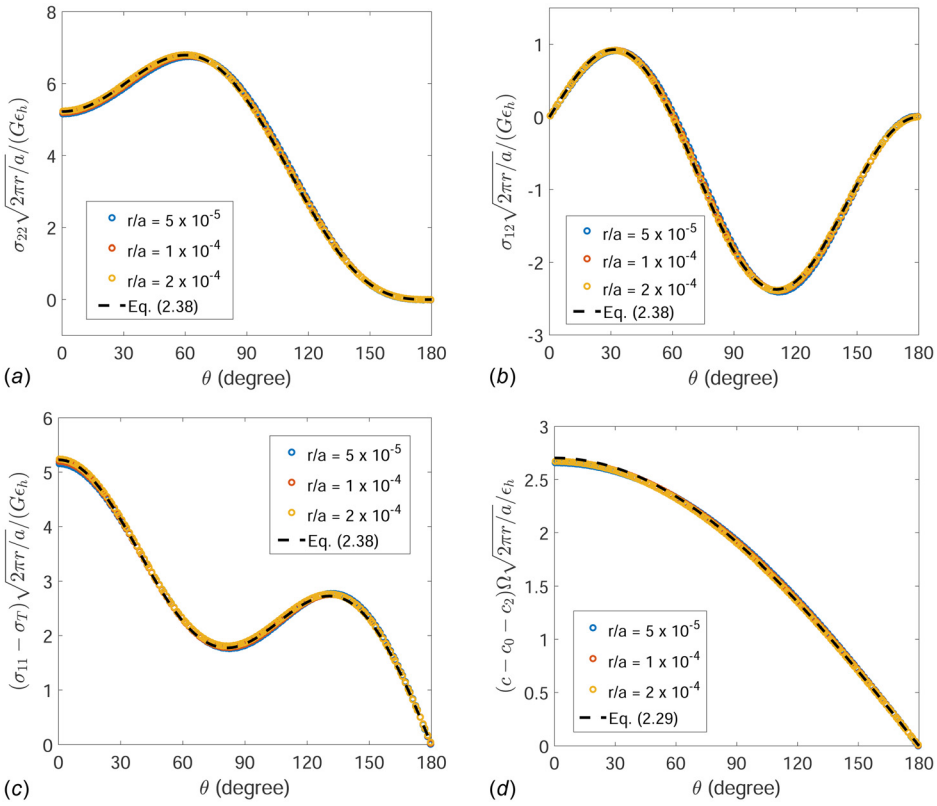

Fig. 3 Numerical results for the angular distributions of the stress components (*a*)–(*c*) and solvent concentration (*d*) around the crack tip at $t/\tau = 10^{-4}$, in comparison with the asymptotic predictions, for the immersed case with $h/a = 10$ and $\nu = 0.24$

by Bouklas et al. [29]. For both the immersed and not-immersed cases, the numerical results approach the theoretical values at the short-time and long-time limits represented by the horizontal dashed and dotted lines in Fig. 5(*a*). The T-stress in Fig. 5(*b*) is negative for both cases, with the magnitude decreasing over time. At short time, the magnitude of T-stress is higher for the immersed case than the not-immersed case. At the long time limit, the T-stress approaches to the elastic limits, $T_\infty = -2G\varepsilon_h/(1-\nu)$, with $\nu = 0.24$ for the immersed case and $\nu = 0.5$ for the not-immersed case. Figure 5(*c*) shows that the chemical potential at the crack tip for the not-immersed case is negative, first increasing and then decreasing over time, with a long-time limit as predicted in Sec. 3 by the method of superposition ($\mu_\infty = -1.95\Omega G\varepsilon_h$). Two additional parameters for the chemical potential, corresponding to the square root term (μ_3) for the immersed case and the linear term (μ_4) for the not-immersed case, are shown in Fig. 5(*d*), both decreasing over time and vanishing at the long-time limit as expected for a constant chemical potential in the equilibrium state. Moreover, Hui et al. [31] predicted that for short-time ($t/\tau \ll 1$), $\mu_3 \sim \Omega K_{I0}/\sqrt{D^* t}$, which agrees closely with the numerical results for the immersed case for $t/\tau < 1$. For the not-immersed case, the numerical results (Fig. 5(*d*)) suggest that $\mu_4 \sim \Omega K_{I0}(D^* t)^{-0.75}$ at short time ($t/\tau < 1$).

4.2 Transient Full-Field Analysis. The full-field time evolution of the chemical potential and solvent concentration in a center-cracked specimen is shown in Fig. 6. Upon loading, the chemical potential immediately becomes inhomogeneous around the crack where the solvent concentration remains homogeneous (except for an infinitesimal region near the crack tip). The gradient of chemical potential drives solvent diffusion so that solvent concentration increases ahead of the crack tip. Meanwhile, solvent diffusion occurs also from the outer edges for the immersed specimen. Eventually, after a sufficiently long-time ($t/\tau \gg 1$), the chemical potential becomes homogeneous ($\mu = 0$) as the specimen reaches chemical equilibrium with the external solution, whereas solvent concentration is inhomogeneous near the crack as a result of inhomogeneous stress and deformation by the condition of mechanical equilibrium. The overall behavior is similar to the results by Bouklas et al. [29].

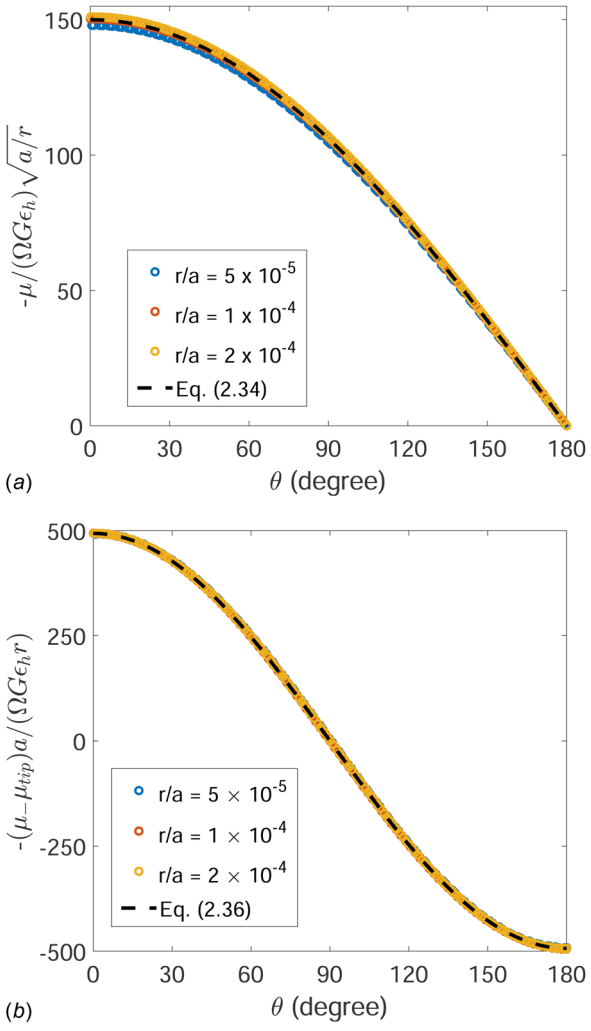

Fig. 4 Angular distributions of the chemical potential for the immersed (*a*) and not-immersed (*b*) cases ($t/\tau = 10^{-4}$, $h/a = 10$ and $\nu = 0.24$)

Figure 7(*a*) shows that the chemical potential ahead of the crack tip follows the poroelastic crack-tip solution in Eq. (2.34) ($\mu \sim r^{1/2}$) up to a distance proportional to the diffusion length ($l_t/a = \sqrt{t/\tau}$). For $r > l_t$, the chemical potential transitions to follow an elastic solution with $\mu \sim r^{-1/2}$ until $r \sim a$. As noted in a previous study [16], by assuming a constant solvent concentration ($c = c_0$) and incompressibility ($\nu = 0.5$), the chemical potential can be obtained from the elastic crack-tip solution as

$$\mu = -\frac{\Omega K_\infty}{\sqrt{2\pi r}}\cos\frac{\theta}{2} \tag{4.1}$$

where K_∞ is the applied stress intensity factor in the far field. It is found that $K_\infty = K_{I0}$ for the center-cracked specimen, corresponding to a linearly elastic specimen with $\nu = 0.5$. For short time ($t/\tau \ll 1$), Hui et al. [31] predicted a self-similar form for the transient evolution of the chemical potential as

$$\mu = -\frac{\Omega K_{I0}}{\sqrt{2\pi r}}\operatorname{erf}\left(\frac{r}{2\sqrt{D^* t}}\right)\cos\frac{\theta}{2} \tag{4.2}$$

which reduces to Eq. (4.1) for $r > 2l_t$. For $r \ll l_t$, the leading term in Taylor's expansion of Eq. (4.2) is identical to Eq. (2.34), with $\mu_3 = -\Omega K_{I0}/\sqrt{2\pi^2 D^* t}$ as shown in Fig. 5(*d*). Thus, by rescaling the chemical potential as $\mu\sqrt{l_t}/(\Omega K_{I0})$ and the distance as r/l_t in Fig. 7(*b*), the numerical results for $t/\tau < 1$ nearly collapse onto one curve except for the far field ($r > a$). The transition from the poroelastic crack-tip field ($\mu \sim r^{1/2}$) to the elastic field ($\mu \sim r^{-1/2}$) is captured closely by Eq. (4.2), except for the case with an extremely short time ($t/\tau = 10^{-8}$). By Eq. (4.2), the minimum chemical potential is predicted at $r \approx 2l_t$, directly ahead of the crack tip ($\theta = 0$). For $t/\tau > 1$, the elastic crack-tip field ceases to exist, while the poroelastic field extends further away from the crack tip to directly interact with the far field. Eventually, the chemical potential becomes zero everywhere as shown in Fig. 6.

For a not-immersed specimen, Fig. 8 shows that the chemical potential ahead of the crack tip follows the poroelastic crack-tip solution in Eq. (2.36) up to a distance proportional to the diffusion length. Strictly, the elastic crack-tip solution for the chemical potential in Eq. (4.1) does not satisfy the zero-flux condition on the crack faces. Thus, it appears that the elastic crack-tip field does not exist theoretically for the not-immersed case. However, the numerical results in Fig. 8 suggest that the chemical potential follows the elastic solution for $2l_t < r < a$ ahead of the crack tip in the not-immersed case, similar to the immersed case, although the angular distribution of the chemical potential may be different from Eq. (4.1). For $t/\tau > 1$, the poroelastic crack tip field interacts with the far field, and the chemical potential eventually becomes a nonzero constant ($\mu_\infty = -1.95\Omega G\varepsilon_h$) everywhere.

4.3 Energy Release Rate. By the modified J-integral in Eq. (2.43), which is path independent as shown in previous studies [16,17,29], we calculate the crack-tip energy release rate (J^*) in the poroelastic center-cracked specimen. Alternatively, the

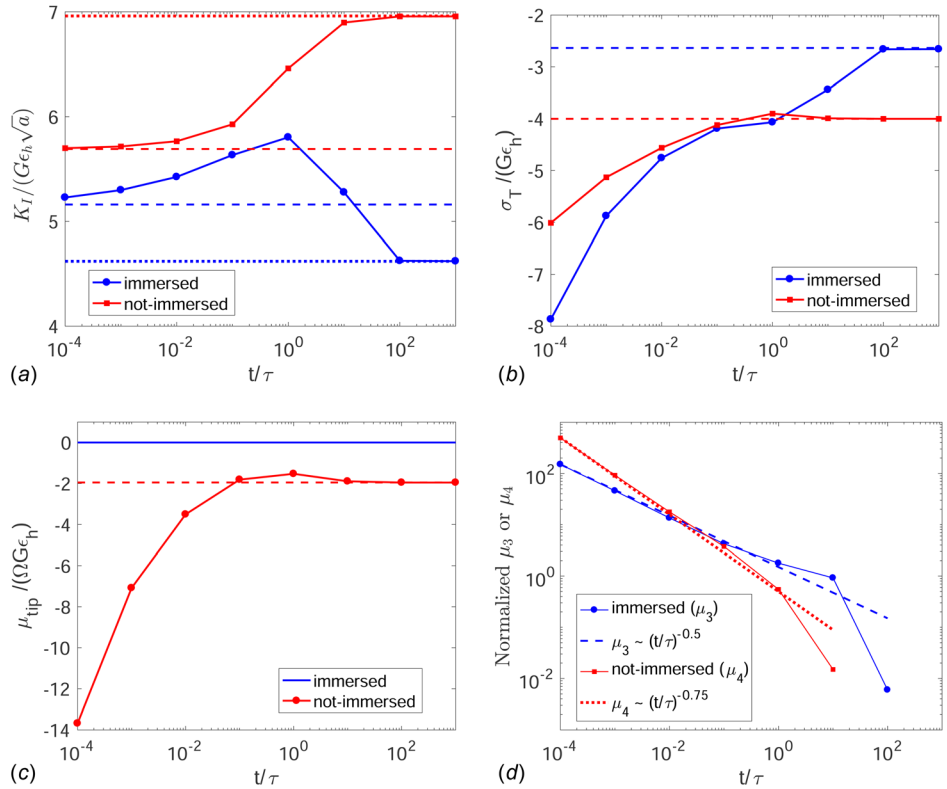

Fig. 5 The normalized crack-tip parameters versus the normalized time for center-cracked specimens (immersed and not-immersed) with $h/a = 10$ and $\nu = 0.24$: (*a*) stress intensity factor, (*b*) T-stress, (*c*) chemical potential at the crack tip, and (*d*) additional parameters for chemical potential (normalized as $\mu_3\sqrt{a}/(\Omega G\varepsilon_h)$ and $\mu_4 a/(\Omega G\varepsilon_h)$)

crack-tip energy release rate can also be calculated using Eq. (2.45) with the time-dependent stress intensity factor in Fig. 5(*a*). Similar to the stress intensity factor, the energy release rate is a function of time for a stationary crack, as noted in Eq. (3.5), with short-time and long-time limits summarized in Table 1. Figure 9(*a*) shows the energy release rate normalized by the instantaneous elastic value as a function of the normalized time (t/τ) for both the immersed and not-immersed specimens under

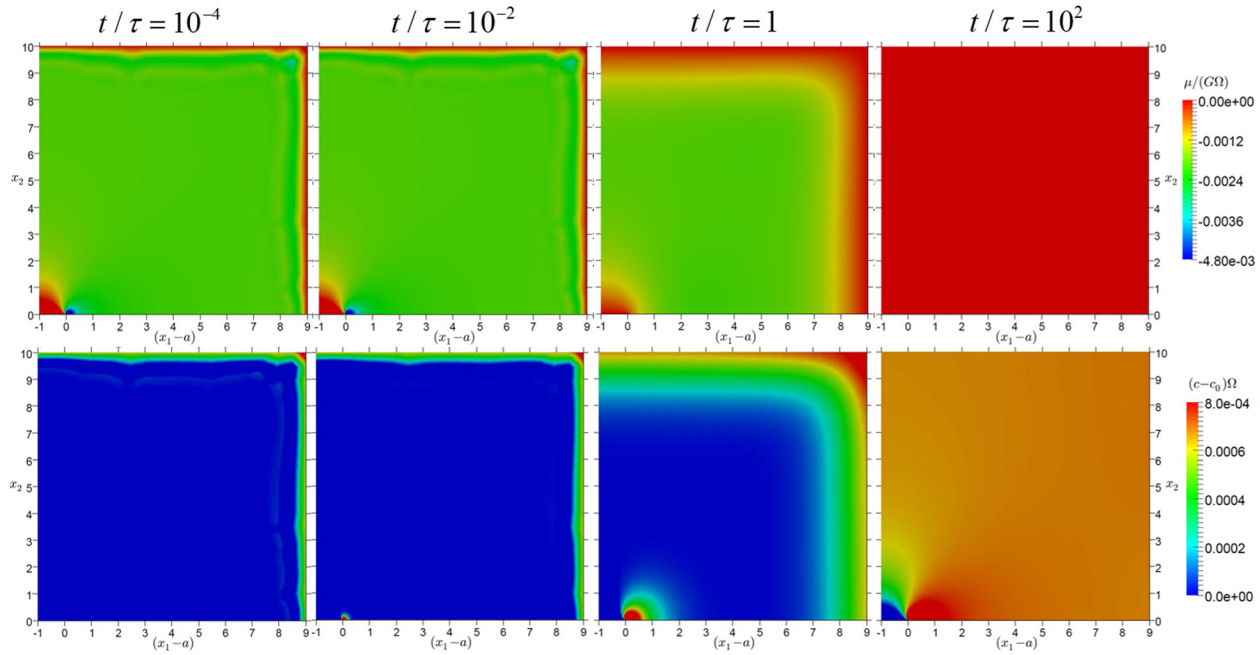

Fig. 6 Time evolution of chemical potential (upper row) and solvent concentration (lower row) in an immersed center-cracked specimen (showing one quarter only) with $\varepsilon_h = 0.001$, $h/a = 10$ and $\nu = 0.24$

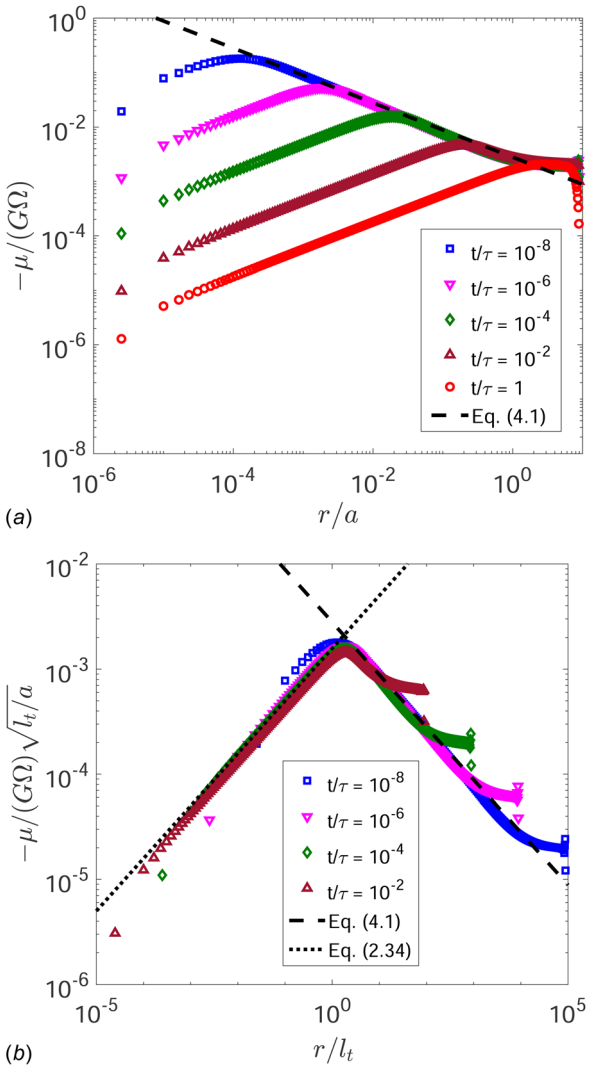

Fig. 7 Chemical potential straight ahead of the crack tip at different times for an immersed center-cracked specimen with $\varepsilon_h = 0.001$, $h/a = 10$ and $\nu = 0.24$

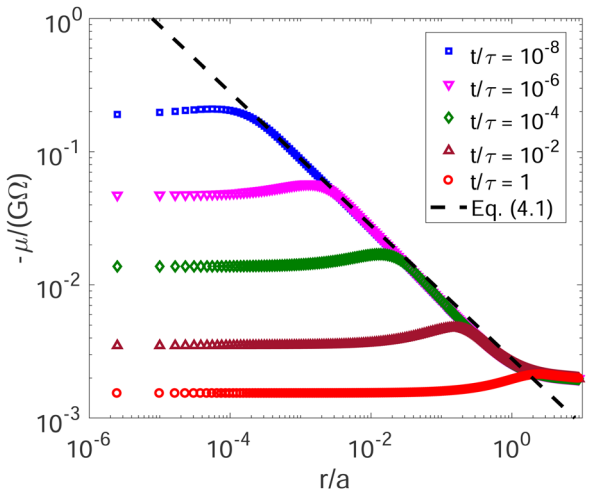

Fig. 8 Chemical potential straight ahead of the crack tip at different times for a not-immersed center-cracked specimen with $\varepsilon_h = 0.001$, $h/a = 10$ and $\nu = 0.24$

displacement-controlled loading with $J_0 = 4\pi\xi_{ue}^2 G\varepsilon_h^2 a$. For the not-immersed case, the normalized energy release rate increases monotonically over time, from the short-time limit ($J^*(t \to 0^+) = J_0$) to the long-time limit ($J^*(t \to \infty) = 1.496J_0$). For the immersed case, however, the normalized energy release rate first increases and then decreases, approaching a long-time limit ($J^*(t \to \infty) = 0.658J_0$) that is smaller than the short-time limit ($J^*(t \to 0^+) = 0.821J_0$). Similar results were obtained previously by Bouklas et al. [29] based on a nonlinear theory, although in principle the short-time and long-time limits are applicable only for the linear theory.

Figure 9(*b*) shows the normalized energy release rates under load control with $K_{I0} = \xi_{\sigma e}\sigma_h\sqrt{\pi a}$ and $J_0 = \pi\xi_{\sigma e}^2\sigma_h^2 a/(4\,G)$. For the not-immersed case, the behavior is similar for both displacement and load controlled conditions, except for a slightly different long-time limit ($J^*(t \to \infty) = 1.52J_0$) as discussed in Sec. 3. On the other hand, the behavior for the immersed case is very different under load control. While the short-time limit is the same for both displacement and load control, the long-time limits are different for the immersed case. In contrast to the nonmonotonic variation under displacement control (Fig. 9(*a*)), the crack-tip energy release rate for the immersed case increases monotonically under load control, approaching the same long-time limit as for the not-immersed case. Thus, under different loading conditions, the fracture behavior could be different for the immersed specimens.

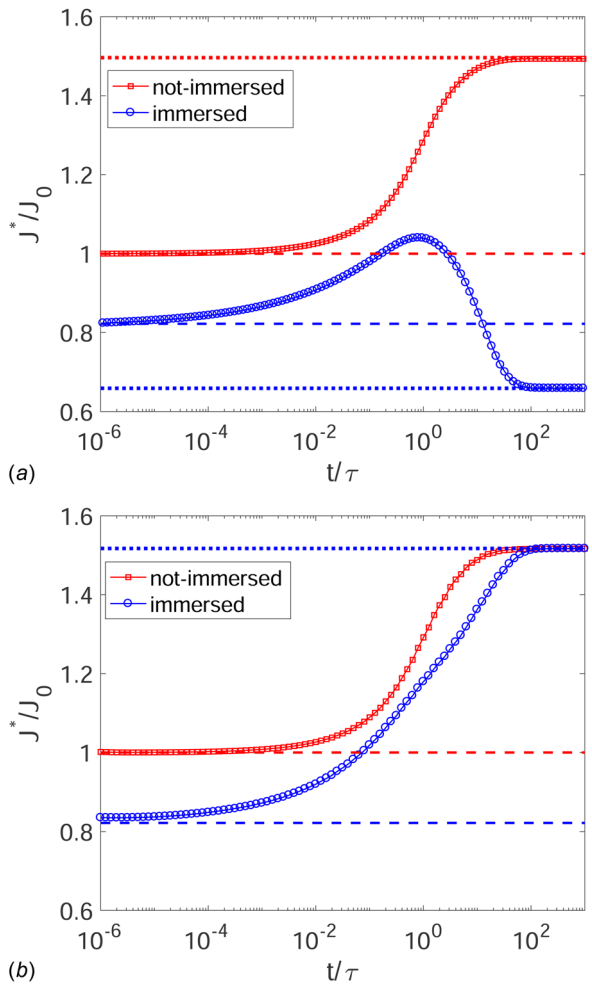

Fig. 9 Energy release rate (J^*), normalized by J_0, as a function of the normalized time (t/τ) for immersed and not-immersed center-cracked specimens with $h/a = 10$ and $\nu = 0.24$: (*a*) Under displacement control and (*b*) under load control. The horizontal dashed and dotted lines are the short-time and long-time limits.

Previously, Wang and Hong [28] predicted similar results for impermeable cracks (not immersed) using a nonlinear visco-poroelastic model, where the crack-tip energy release rate was calculated using a cohesive zone model. More recently, based on a linear poroviscoelastic model, Yang and Lin [33] reported similar results for both permeable (immersed) and impermeable (not immersed) cracks under load control, and they too used a cohesive zone model to calculate the crack-tip energy release rate. The present study shows that the crack-tip energy release rate in a poroelastic material can be calculated by the modified J-integral method, without using a cohesive zone model. On the other hand, a poroelastic cohesive zone model [16] could be used to simulate rate-dependent fracture process for both crack initiation and propagation.

4.4 Delayed Fracture. As a hypothetical fracture criterion for polymer gels, a stationary crack would start growing once the crack-tip energy release rate (J^*) reaches a critical value that may be considered as the intrinsic fracture toughness (Γ) of the gel. Since J^* depends on time (Fig. 9), the crack may grow immediately or after a time delay or may not grow at all, depending on the applied load (either displacement or load control) as well as the chemical boundary condition (immersed or not-immersed). According to the numerical results in Fig. 9, except for the immersed case under displacement-controlled loading, the energy release rate (J^*) increases monotonically from the short-time limit to the long-time limit. In these cases, the crack would grow immediately if the short-time limit of the energy release rate is greater than the fracture toughness ($J^*(t \to 0^+) > \Gamma$) but would never grow if the long-time limit is lower than the fracture toughness ($J^*(t \to \infty) < \Gamma$), while delayed crack growth may be expected if $J^*(t \to 0^+) < \Gamma < J^*(t \to \infty)$. Taking J_0 as the loading parameter, which is proportional to the square of the applied displacement or traction ($J_0 \sim \varepsilon_h^2$ or σ_h^2), the delay time may be predicted by setting $J^*(t) = \Gamma$ in Eq. (3.5). Figure 10 illustrates the possible scenario of delayed fracture under load control for both the immersed and not-immersed cases. For a center-cracked specimen with $h/a = 10$ and $\nu = 0.24$, the crack would never grow if $J_0/\Gamma < 0.66$ (inverse of the long-time limit), immersed or not. For the not-immersed case, delayed fracture would occur if $0.66 < J_0/\Gamma < 1$, with the delay time decreasing as the applied load (J_0) increases; the crack grows immediately if $J_0/\Gamma > 1$. For the immersed case, the crack grows immediately if $J_0/\Gamma > 1.22$ (inverse of the short-time limit). Hence, the gel would appear to be tougher when immersed (poroelastic toughening). Under the same loading ($0.66 < J_0/\Gamma < 1$), the delay time would be longer for the immersed case than not-immersed case.

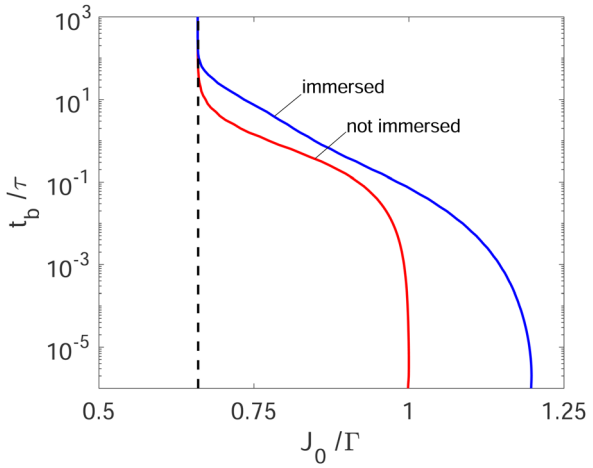

Fig. 10 Delay time for onset of crack growth under load control for the immersed and not-immersed specimens

Experimentally, delayed fracture has been observed in polymer gels [18–20] as well as many other materials [21–27]. For polymer gels, delayed fracture may result from several molecular processes, such as thermally activated crack nucleation, stress-enhanced bond rupture and dissociation, viscoelasticity (creep) and poroelasticity (solvent diffusion). Bonn et al. [18] proposed a crack nucleation model for their three-point bending experiments with un-cracked gel specimens, which predicted a power-law dependence of the activation energy on the applied force ($E_{\text{act}} \sim 1/\sigma^{2d-2}$ with $1 < d \leq 2$) and an exponential dependence of the mean breaking time on the activation energy ($t_b \sim \exp(E_{\text{act}}/k_BT)$). Skrzeszewska et al. [19] found that the nucleation model (with $d = 3$) could not explain their experiments with a physical gel fractured under a constant shear stress and proposed a stress-enhanced crosslink dissociation model with a rupture time decreasing exponentially with increasing stress ($t_b \sim \exp(-3.75\sigma/G)$). Based on a nonlinear visco-poroelastic model, Wang and Hong [28] suggested that the delay time depends on the size of a pre-existing crack in a similar way as diffusion-limited processes (a poroelastic effect). By assuming a specific size distribution of microcracks, they proposed a statistical theory for the lifetime prediction of a swollen gel. Recently, Tang et al. [20] conducted fracture experiments of hydrogels using pre-cracked specimens. They observed delayed fracture when the applied energy release rate was subcritical but greater than a threshold value, while the delay time increased as the applied energy release rate decreased. This observation is qualitatively consistent with Fig. 10, where the critical energy release rate for instantaneous crack growth is set by the short-time limit ($J^*(t \to 0^+) > \Gamma$) and the threshold for delayed fracture is set by the long-time limit ($J^*(t \to \infty) > \Gamma$). In between, the delay time decreases sharply with increasing load (J_0) and can be written as

$$t_b = \frac{a^2}{D^*} f\left(\frac{J_0}{\Gamma}, \nu\right) \tag{4.3}$$

where the dimensionless function $f(J_0/\Gamma, \nu)$ depends on the specimen geometry and the chemo-mechanical loading conditions as shown in Fig. 10 for center-crack specimens.

5 Summary

Based on a linear poroelastic formulation, an asymptotic analysis of the transient crack-tip fields is developed for stationary cracks in polymer gels. A center crack model is studied in detail, comparing numerical results by a finite element method to the asymptotic analysis. The time evolution of the crack-tip parameters is determined as a result of solvent diffusion coupled with elastic deformation of the gel. A modified J-integral method is used to calculate the crack-tip energy release rate. The short-time and long-time limits are obtained for the poroelastic stress intensity factor and the crack-tip energy release rate under different chemo-mechanical boundary conditions (immersed versus not-immersed, displacement versus load controlled). The results show that, under displacement-controlled loading, the crack-tip energy release rate increases monotonically over time for the not-immersed case, but for the immersed case it increases first and then decreases, with a long-time limit lower than the short-time limit. Under load control, the energy release rate increases over time for both immersed and not-immersed cases, with different short-time limits but the same long-time limit. These results suggest that onset of crack growth may be delayed until the crack-tip energy release rate reaches a critical value if the applied displacement or traction is subcritical but greater than a threshold, qualitatively consistent with experiments.

Funding Data

- The National Science Foundation (Grant No. CMMI-1538658).

Appendix A: Formulation of a Finite Element Method

The solution to a poroelastic initial/boundary value problem consists of a vector field of displacement and a scalar field of chemical potential, $\mathbf{u}(\mathbf{x}, t)$ and $\mu(\mathbf{x}, t)$. Similar to previous works [17,29], the weak form of Eqs. (2.4) and (2.5) is obtained by using test functions $\delta\mathbf{u}(\mathbf{x})$ and $\delta\mu(\mathbf{x})$ with the divergence theorem, namely

$$\int_{V_0} \sigma_{ij}\delta u_{i,j} dV = \int_{S_0} \tau_i \delta u_i dS \tag{A1}$$

$$\int_{V_0} \left(\frac{\partial c}{\partial t}\delta\mu - j_k \delta\mu_{,k}\right) dV = \int_{S_0} \omega\delta\mu dS \tag{A2}$$

A backward Euler scheme is used to integrate Eq. (A2) over time, namely

$$\int_{V_0} \left(\frac{c^{t+\Delta t} - c^t}{\Delta t}\delta\mu - j_k^{t+\Delta t}\delta\mu_{,k}\right) dV = \int_{S_0} \omega^{t+\Delta t}\delta\mu dS \tag{A3}$$

Combining Eqs. (A1) and (A3), we obtain

$$\int_{V_0} (\sigma_{ij}\delta u_{i,j} - c\delta\mu + \Delta t j_k \delta\mu_{,k}) dV = \int_{S_0} (\tau_i \delta u_i - \omega\Delta t\delta\mu) dS - \int_{V_0} c^t \delta\mu dV \tag{A4}$$

where the superscripts are omitted for all the terms at the current time-step $(t + \Delta t)$ and c^t is the solvent concentration at the previous time-step.

The displacement field and the chemical potential are discretized as

$$\mathbf{u} = \mathbf{N}^u \mathbf{u}^n \text{ and } \mu = \mathbf{N}^\mu \boldsymbol{\mu}^n \tag{A5}$$

where $\mathbf{u}^n$ and $\boldsymbol{\mu}^n$ are the nodal values, $\mathbf{N}^u$ and $\mathbf{N}^\mu$ are the corresponding shape functions for the displacements and the chemical potential, respectively. The test functions are discretized in the same way

$$\delta\mathbf{u} = \mathbf{N}^u \delta\mathbf{u}^n \text{ and } \delta\mu = \mathbf{N}^\mu \delta\boldsymbol{\mu}^n \tag{A6}$$

The stress, solvent concentration and flux are evaluated at the integration points with Eqs. (2.1)–(2.3) and (2.6). Taking the gradients of the discretized displacements and chemical potential, we obtain

$$\nabla\mathbf{u} = \mathbf{B}^u \mathbf{u}^n \text{ and } \nabla\mu = \mathbf{B}^\mu \boldsymbol{\mu}^n \tag{A7}$$

where $\mathbf{B}^u$ and $\mathbf{B}^\mu$ are the gradients of the corresponding shape functions for the displacement and chemical potential fields. In this formulation, different shape functions are allowed for the discretization of the displacement and chemical potential. Following the previous works [17,29], the two-dimensional 8**u**4p Taylor–Hood elements with biquadratic serendipity interpolation for displacement and bilinear interpolation for chemical potential are used to alleviate numerical oscillations.

Upon discretization, the weak form in Eq. (A4) leads to a system of linear equations

$$\mathbf{K}\mathbf{d} = \mathbf{f} \tag{A8}$$

where $\mathbf{d} = (\mathbf{u}^n, \boldsymbol{\mu}^n)^{\mathrm{T}}$, $\mathbf{f}$ is the external force vector, and $\mathbf{K}$ is the stiffness matrix. More specifically, the external force components are given by

$$f_i^{u,m} = \int_{S_0} \tau_i N^{u,m} dS \tag{A9}$$

$$f^{\mu,m} = -\int_{S_0} \omega\Delta t N^{\mu,m} dS - \int_{V_0} c^t N^{\mu,m} dV \tag{A10}$$

where m indicates the node number. The stiffness matrix can be written as

$$\mathbf{K} = \begin{bmatrix} K^{uu} & K^{u\mu} \\ K^{\mu u} & K^{\mu\mu} \end{bmatrix} \tag{A11}$$

where the components for each pair of nodes (m, n) and degrees-of-freedom (i, k) are

$$K_{ik}^{uu,mn} = \int_{V_0} B_j^{u,m} \frac{\partial\sigma_{ij}}{\partial u_{k,l}} B_l^{u,n} dV \tag{A12a}$$

$$K_i^{u\mu,mn} = K_i^{\mu u,nm} = -\frac{1}{\Omega}\int_{V_0} B_i^{u,m} N^{\mu,n} dV \tag{A12b}$$

$$K^{\mu\mu,mn} = -M_0\Delta t \int_{V_0} B_i^{\mu,m} B_i^{\mu,n} dV \tag{A12c}$$

In Eq. (A12*a*), the derivative of the stress gives the isotropic elasticity tensor, namely

$$\frac{\partial\sigma_{ij}}{\partial u_{k,l}} = G\left(\delta_{ik}\delta_{jl} + \delta_{il}\delta_{jk} + \frac{2\nu}{1-2\nu}\delta_{ij}\delta_{kl}\right) \tag{A13}$$

Thus, the stiffness matrix is symmetric for linear poroelasticity, which is not the case for the nonlinear formulation [29]. A standard symmetric solver is used to solve Eq. (A8) at each time-step.

Appendix B: Short-Time Limit for the Immersed Case

The poroelastic stress intensity factor at the short-time limit was given by Eq. (89) in Atkinson and Craster [30]:

$$K_I(t \to 0^+) = \frac{K_e}{[N_+(0) - \bar{\eta}d]} \tag{B1}$$

where K_e is the corresponding elastic stress intensity factor and $\bar{\eta} = (1-\nu)/(2(\nu_u - \nu))$ with ν and ν_u being the drained and undrained Poisson's ratios. In the present study, $\nu_u = 0.5$ by the assumption of molecular incompressibility for both the polymer and the solvent.

Two split functions, $N_-(\xi)$ and $N_+(\xi)$, are given by Eqs. (185) and (188) in Atkinson and Craster [30]

$$\ln\left[\frac{N_-(\xi)}{-N_0}\right] = -\frac{1}{\pi}\int_0^1 \arctan\left[\frac{p(1-p^2)^{1/2}}{p^2 - \bar{\eta}}\right]\frac{dp}{p + i\xi} \tag{B2}$$

$$\ln[N_+(\xi)] = -\frac{1}{\pi}\int_0^1 \arctan\left[\frac{p(1-p^2)^{1/2}}{p^2 - \bar{\eta}}\right]\frac{dp}{p - i\xi} \tag{B3}$$

with $N_0 = (1 - 2\bar{\eta})/2$. By Eq. (B3), we obtain

$$N_+(0) = \sqrt{\frac{1-\nu}{1-\nu_u}} \tag{B4}$$

Finally, the expression for d is given by Eq. (202) in Atkinson and Craster [30]

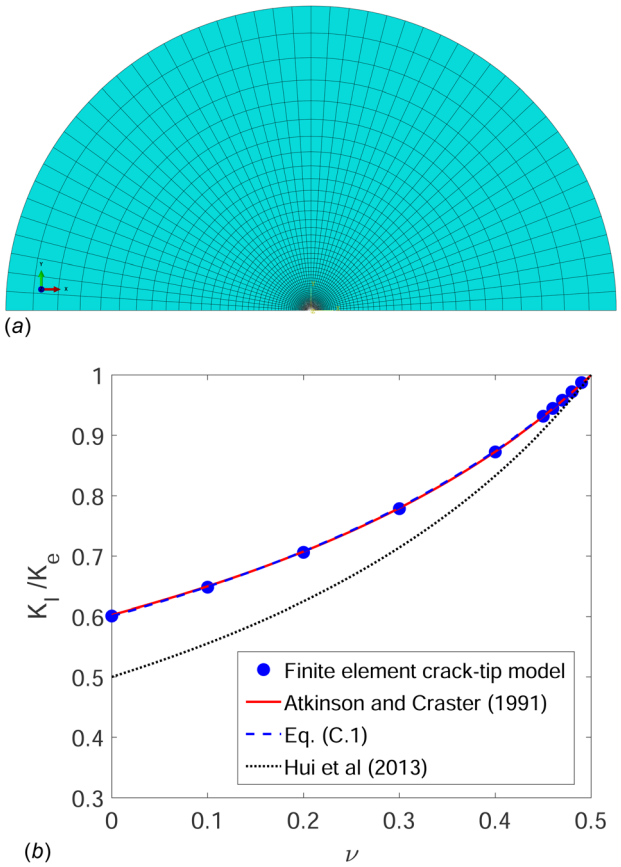

Fig. 11 (*a*) Finite element mesh for the crack tip model and (*b*) effect of Poisson's ratio on the crack-tip stress intensity factor, comparing the numerical results with analytical predictions

$$d = -\frac{1}{\pi}\int_0^1 \frac{dy}{y^{1/2}(1-y)^{1/2}}\left[\frac{1}{N_-(-iy)} - N_+(0)\bar{\eta}\right] \tag{B5}$$

which can be evaluated by numerical integration. The results are shown in Fig. 11 in comparison with the finite element analysis.

Appendix C: A Crack-Tip Model for the Short-Time Limit

For the short-time limit ($t \to 0^+$), the characteristic diffusion length is much smaller than the crack length ($l_t = \sqrt{D^* t} \ll a$), and an elastic crack-tip field exists as the transition field (see Fig. 7) between the poroelastic crack-tip field and the far field for the immersed case. Similar to the previous study for steady-state crack growth [17], a crack-tip model (Fig. 11(*a*)) can be used to determine the poroelastic crack tip field at the short-time limit. A similar model was used by Hui et al. [31], where a very fine mesh was used to suppress numerical oscillations with standard elements in ABAQUS. By using Taylor–Hood elements in the present study, a relatively coarse mesh can be used except for the crack-tip region, where the mesh becomes increasingly finer in order to accurately resolve the singular stress and concentration fields.

By symmetry, only half of the domain around the crack tip is modeled (Fig. 11(*a*)). A circular outer boundary is arbitrarily set at $r = 1000$ as the normalized domain size. The displacement and chemical potential corresponding to the elastic crack-tip field with a stress intensity factor K_e are prescribed at the outer boundary. The symmetry boundary conditions are applied straight ahead of the crack tip ($\theta = 0$), whereas the crack face ($\theta = \pi$) is traction free with zero chemical potential. For the short-time limit, we solve the transient problem up to a time $t_{\max} \ll r_{\max}^2/D^*$. With normalized values, $r_{\max} = 1000$ and $D^* = 10^6$, we set $t_{\max} = 10^{-6}$ in our calculations. The crack-tip energy release rate (J^*) is calculated by the modified J-integral method, which is path independent and remains a constant over time within the short-time limit ($t < t_{\max}$). Then, by Eq. (2.45), the poroelastic crack-tip stress intensity factor (K_I) is determined, which is also a constant at the short-time limit.

By dimensional considerations, the poroelastic crack-tip stress intensity factor must be linearly proportional to K_e that is applied at the outer boundary, with a proportionality depending on the Poisson's ratio. Figure 11(*b*) shows the normalized stress intensity factor (K_I/K_e) as a function of Poisson's ratio at the short-time limit. The finite element results from the crack-tip model agree very closely with the semi-analytical solution by Atkinson and Craster [30], which can be fitted by a simple function as:

$$K_I(t \to 0^+) = K_e\left[\frac{1}{2(1-\nu)}\right]^{\alpha} \tag{C1}$$

with $\alpha \approx 0.735$. On the other hand, Hui et al. [31] predicted a different short-time limit with $\alpha = 1$, which apparently underestimates the poroelastic stress intensity factor.

Correspondingly, the crack-tip energy release rate at the short-time limit depends on Poisson's ratio as

$$J^*(t \to 0^+) = J_e\left[\frac{1}{2(1-\nu)}\right]^{2\alpha-1} \tag{C2}$$

where $J_e = K_e^2/(4G)$ is the applied energy release rate. For the immersed case, $J^*(t \to 0^+) < J_e$, and the difference is due to energy dissipation by solvent diffusion within the domain.

References

[1] Drury, J. L., and Mooney, D. J., 2003, "Hydrogels for Tissue Engineering: Scaffold Design Variables and Applications," Biomaterials, **24**(24), pp. 4337–4351.
[2] Langer, R., 2006, "Biomaterials for Drug Delivery and Tissue Engineering," MRS Bull., **31**(6), pp. 477–485.
[3] Peppas, N. A., Hilt, J. Z., Khademhosseini, A., and Langer, R., 2006, "Hydrogels in Biology and Medicine: From Molecular Principles to Bionanotechnology," Adv. Mater., **18**(11), pp. 1345–1360.
[4] Calvert, P., 2009, "Hydrogels for Soft Machines," Adv. Mater., **21**(7), pp. 743–756.
[5] Suo, Z., 2012, "Mechanics of Stretchable Electronics and Soft Machines," MRS Bull., **37**(3), pp. 218–225.
[6] Yuk, H., Lin, S. T., Ma, C., Takaffoli, M., Fang, N. X., and Zhao, X., 2017, "Hydraulic Hydrogel Actuators and Robots Optically and Sonically Camouflaged in Water," Nat. Commun., **8**, p. 14230.
[7] Yang, C., and Suo, Z., 2018, "Hydrogel Ionotronics," Nat. Rev. Mater., **3**(6), pp. 125–142.
[8] Gong, J. P., Katsuyama, Y., Kurokawa, T., and Osada, Y., 2003, "Double-Network Hydrogels With Extremely High Mechanical Strength," Adv. Mater., **15**(14), pp. 1155–1158.
[9] Sun, J. Y., Zhao, X. H., Illeperuma, W. R. K., Chaudhuri, O., Oh, K. H., Mooney, D. J., Vlassak, J. J., and Suo, Z., 2012, "Highly Stretchable and Tough Hydrogels," Nature, **489**(7414), pp. 133–136.
[10] Zhao, X., 2014, "Multi-Scale Multi-Mechanism Design of Tough Hydrogels: Building Dissipation Into Stretchy Networks," Soft Matter, **10**(5), pp. 672–687.
[11] Long, R., and Hui, C. Y., 2016, "Fracture Toughness of Hydrogels: Measurement and Interpretation," Soft Matter, **12**(39), pp. 8069–8086.
[12] Creton, C., 2017, "50th Anniversary Perspective: Networks and Gels: Soft but Dynamic and Tough," Macromolecules, **50**(21), pp. 8297–8316.
[13] Lefranc, M., and Bouchaud, E., 2014, "Mode I Fracture of a Biopolymer Gel: Rate-Dependent Dissipation and Large Deformations Disentangled," Extreme Mech. Lett., **1**, pp. 97–103.
[14] Forte, A. E., D'Amico, F., Charalambides, M. N., Dini, D., and Williams, J. G., 2015, "Modelling and Experimental Characterisation of the Rate Dependent Fracture Properties of Gelatine Gels," Food Hydrocolloid, **46**, pp. 180–190.
[15] Baumberger, T., Caroli, C., and Martina, D., 2006, "Solvent Control of Crack Dynamics in a Reversible Hydrogel," Nat. Mater., **5**(7), pp. 552–555.
[16] Noselli, G., Lucantonio, A., McMeeking, R. M., and DeSimone, A., 2016, "Poroelastic Toughening in Polymer Gels: A Theoretical and Numerical Study," J. Mech. Phys. Solids, **94**, pp. 33–46.
[17] Yu, Y., Landis, C. M., and Huang, R., 2018, "Steady-State Crack Growth in Polymer Gels: A Linear Poroelastic Analysis," J. Mech. Phys. Solids, **118**, pp. 15–39.

[18] Bonn, D., Kellay, H., Prochnow, M., Ben-Djemiaa, K., and Meunier, J., 1998, "Delayed Fracture of an Inhomogeneous Soft Solid," Science, **280**(5361), pp. 265–267.
[19] Skrzeszewska, P. J., Sprakel, J., de Wolf, F. A., Fokkink, R., Stuart, M. A. C., and van der Gucht, J., 2010, "Fracture and Self-Healing in a Well-Defined Self-Assembled Polymer Network," Macromolecules, **43**(7), pp. 3542–3548.
[20] Tang, J., Li, J., Vlassak, J. J., and Suo, Z., 2017, "Fatigue Fracture of Hydrogels," Extreme Mech. Lett., **10**, pp. 24–31.
[21] Petch, N. J., and Stables, P., 1952, "Delayed Fracture of Metals Under Static Load," Nature, **169**(4307), pp. 842–843.
[22] Pearson, S., 1956, "Delayed Fracture of Sintered Alumina," P. Phys. Soc. B, **69**(12), pp. 1293–1296.
[23] Knauss, W. G., 1970, "Delayed Failure—the Griffith Problem for Linearly Viscoelastic Materials," Int. J. Fract. Mech., **6**(1), pp. 7–20.
[24] Sprakel, J., Lindstrom, S. B., Kodger, T. E., and Weitz, D. A., 2011, "Stress Enhancement in the Delayed Yielding of Colloidal Gels," Phys. Rev. Lett., **106**(24), p. 248303.
[25] Lindstrom, S. B., Kodger, T. E., Sprakel, J., and Weitz, D. A., 2012, "Structures, Stresses, and Fluctuations in the Delayed Failure of Colloidal Gels," Soft Matter, **8**(13), pp. 3657–3664.
[26] Shahidzadeh-Bonn, N., Vie, P., Chateau, X., Roux, J.-N., and Bonn, D., 2015, "Delayed Fracture in Porous Media," Phys. Rev. Lett., **95**(17), p. 175501.
[27] van der Kooij, H. M., Dussi, S., van de Kerkhof, G. T., Frijns, R. A. M., van der Gucht, J., and Sprakel, J., 2018, "Laser Speckle Strain Imaging Reveals the Origin of Delayed Fracture in a Soft Solid," Sci. Adv., **4**(5), p. eaar1926
[28] Wang, X., and Hong, W., 2012, "Delayed Fracture in Gels," Soft Matter, **8**(31), pp. 8171–8178.
[29] Bouklas, N., Landis, C. M., and Huang, R., 2015, "Effect of Solvent Diffusion on Crack-Tip Fields and Driving Force for Fracture of Hydrogels," ASME J. Appl. Mech., **82**(8), p. 081007.
[30] Atkinson, C., and Craster, R. V., 1991, "Plane Strain Fracture in Poroelastic Media," Proc. R. Soc. London. Ser. A, **434**(1892), pp. 605–633.
[31] Hui, C. Y., Long, R., and Ning, J., 2013, "Stress Relaxation Near the Tip of a Stationary Mode I Crack in a Poroelastic Solid," ASME J. Appl. Mech., **80**(2), p. 021014.
[32] Bouklas, N., Landis, C. M., and Huang, R., 2015, "A Nonlinear, Transient Finite Element Method for Coupled Solvent Diffusion and Large Deformation of Hydrogels," J. Mech. Phys. Solids, **79**, pp. 21–43.
[33] Yang, C.-H., and Lin, Y.-Y., 2018, "Time-Dependent Fracture of Mode-I Cracks in Poroviscoelastic Media," Eur. J. Mech. - A/Solids, **69**, pp. 78–87.
[34] Böger, L., Keip, M.-A., and Miehe, C., 2017, "Minimization and Saddle-Point Principles for the Phase-Field Modeling of Fracture in Hydrogels," Comput. Mater. Sci., **138**, pp. 474–485.
[35] Mao, Y., and Anand, L., 2018, "A Theory for Fracture of Polymeric Gels," J. Mech. Phys. Solids, **115**, pp. 30–53.
[36] Hong, W., Zhao, X., Zhou, J., and Suo, Z., 2008, "A Theory of Coupled Diffusion and Large Deformation in Polymeric Gels," J. Mech. Phys. Solids, **56**(5), pp. 1779–1793.
[37] Hong, W., Liu, Z., and Suo, Z., 2009, "Inhomogeneous Swelling of a Gel in Equilibrium With a Solvent and Mechanical Load," Int. J. Solids Struct., **46**(17), pp. 3282–3289.
[38] Kang, M. K., and Huang, R., 2010, "A Variational Approach and Finite Element Implementation for Swelling of Polymeric Hydrogels Under Geometric Constraints," ASME J. Appl. Mech., **77**(6), p. 061004.
[39] Bouklas, N., and Huang, R., 2012, "Swelling Kinetics of Polymer Gels: Comparison of Linear and Nonlinear Theories," Soft Matter, **8**(31), pp. 8194–8203.
[40] Hui, C.-Y., Lin, Y. Y., Chuang, F.-C., Shull, K. R., and Lin, W.-C., 2006, "A Contact Mechanics Method for Characterizing the Elastic Properties and Permeability of Gels," J. Polym. Sci., Part B: Polym. Phys., **44**(2), pp. 359–370.
[41] Hu, Y., Chen, X., Whitesides, G. M., Vlassak, J. J., and Suo, Z., 2011, "Indentation of Polydimethylsiloxane Submerged in Organic Solvents," J. Mater. Res., **26**(6), pp. 785–795.
[42] Craster, R. V., and Atkinson, C., 1992, "Shear Cracks in Thermoelastic and Poroelastic Media," J. Mech. Phys. Solids, **40**(4), pp. 887–924.